Letter

Electric field induced thermal Hall effect of triplons in the quantum dimer magnets $X\mathrm{CuCl_3}$ (X = Tl, K)

Nanse Esaki* and Yutaka Akagi
Department of Physics, Graduate School of Science, The University of Tokyo, 7-3-1 Hongo, Tokyo 113-0033, Japan

Hosho Katsura
Department of Physics, Graduate School of Science, The University of Tokyo, 7-3-1 Hongo, Tokyo 113-0033, Japan;
Institute for Physics of Intelligence, The University of Tokyo, 7-3-1 Hongo, Tokyo 113-0033, Japan;
and Trans-scale Quantum Science Institute, The University of Tokyo, 7-3-1, Hongo, Tokyo 113-0033, Japan

(Received 18 October 2023; accepted 22 July 2024; published 3 September 2024)

We theoretically propose the electric field induced thermal Hall effect of triplons in the quantum dimer magnets $X\mathrm{CuCl_3}$ (X = Tl, K), which exhibit ferroelectricity in the Bose-Einstein condensation phase of triplons. The interplay between ferroelectricity and magnetism in these materials leads to the magnetoelectric effect, i.e., an electric-field induced Dzyaloshinskii-Moriya (DM) interaction between spins on the same dimer. We argue that this intradimer DM interaction breaks the symmetry of the system in the absence of an electric field and gives rise to the thermal Hall effect, which can be detected in experimentally accessible electric and magnetic fields. We also show that the thermal Hall effect can be controlled by changing the strength or direction of the electric field.

DOI: 10.1103/PhysRevResearch.6.L032050

Introduction. Quantum spin systems exhibit a variety of interesting properties that are not present in their classical counterparts. Quantum dimer magnets are such examples, where the neighboring $S = 1/2$ spins form dimers with a spin-singlet ground state and triplet bosonic excitations called triplons. The triplons undergo Bose-Einstein condensation (BEC) when the magnetic field exceeds a critical value [1–10]. In the BEC phase, the ground state of an individual dimer is a coherent superposition of the singlet and triplet states, which breaks the inversion symmetry and can lead to the spontaneous polarization on dimers. In particular, $X\mathrm{CuCl_3}$ (X = Tl, K) is known to exhibit ferroelectricity in the BEC phase, whereas these materials have inversion centers at the center of dimers in the weak magnetic field regime [11–14]. When one applies an electric field in the BEC phase, the spin-dependent polarization can couple with the electric field, inducing the intradimer Dzyaloshinskii-Moriya (DM) interaction [15–27]. It is thus natural to ask whether the transport of triplons in these materials can be significantly affected or controlled by the electric field.

Various transverse transport phenomena associated with the Berry curvature have been proposed for bosonic excitations such as magnons [28–71], photons [72–76], phonons [77–82], and triplons [83–90]. Of particular interest is the thermal Hall effect of magnons induced by the DM interactions that has been observed experimentally [29,31]. By contrast, the thermal Hall effect of triplons has yet to be detected experimentally [89], despite the theoretical prediction for $\mathrm{SrCu_2(BO_3)_2}$ [83,84,87,88].

In this Letter, we propose the electric field induced thermal Hall effect of triplons in $X\mathrm{CuCl_3}$. The magnetic properties of these materials are well described by the isotropic Heisenberg Hamiltonian with DM interactions [3–5,91]. In the absence of an electric field, the system possesses an effective PT symmetry and does not exhibit the thermal Hall effect. We find that an electric field induces intradimer DM interactions breaking this symmetry, thereby leading to the thermal Hall effect. We also show that the magnitude (direction) of the thermal Hall current can be controlled by manipulating the strength (direction) of the electric field. Our numerical results for $\mathrm{TlCuCl_3}$ suggest that the thermal Hall effect in $X\mathrm{CuCl_3}$ can be observed in experimentally attainable electric and magnetic fields.

The model. $X\mathrm{CuCl_3}$ is a three-dimensional interacting dimer system where the $S = 1/2$ spins of $\mathrm{Cu^{2+}}$ ions form dimers due to the strong intradimer interactions [3–5,91] [see Fig. 1 and the Supplemental Material [92]]. The unit cell contains two equivalent dimers, which belong to two different sublattices labeled as 1 and 2 in the following. The spin-1/2 operators $\boldsymbol{S}_l^m(\boldsymbol{R})$ and $\boldsymbol{S}_r^m(\boldsymbol{R})$ denote the left and right spins of the dimer in the unit cell at the position $\boldsymbol{R}$ on the sublattice $m(=1, 2)$, respectively. The lattice unit vectors $\hat{a}$, $\hat{b}$, and $\hat{c}$ correspond to the a, b, and c axes, respectively. The Hamiltonian of the system in a magnetic field $\boldsymbol{H} \| b$ and an electric field $\boldsymbol{E}$ is given by

$$\mathcal{H} = \mathcal{H}_{\mathrm{Hei}} + \mathcal{H}_{\mathrm{DM}} + \mathcal{H}_{\mathrm{ext}}, \tag{1}$$

*Contact author: esaki-nanse0428@g.ecc.u-tokyo.ac.jp

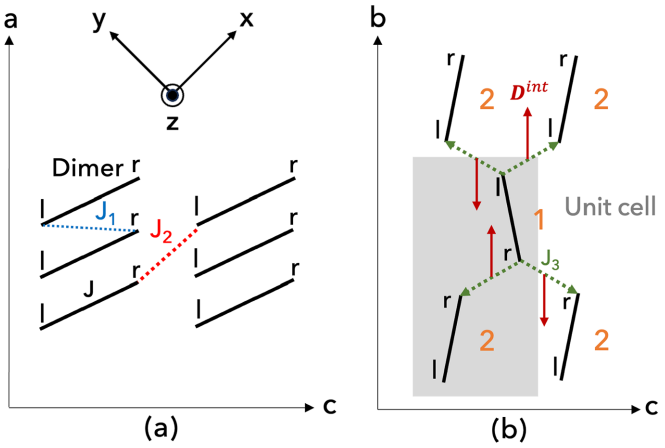

FIG. 1. A schematic picture of dimers and relevant interactions in $X\mathrm{CuCl_3}$: (a) a-c plane; (b) b-c plane. The symbols l and r denote the left and right spins of each dimer. Thick black lines indicate the intradimer exchange coupling J, whereas the dotted blue, red, and green lines denote interdimer exchange couplings J_1, J_2, and J_3, respectively. In (a), x, y, and z axes are indicated. In (b), 1 and 2 are the sublattice indices. The solid brown (dotted green) arrows represent the direction of (sign convention for) $\boldsymbol{D}^{\mathrm{int}}$.

$$\mathcal{H}_{\mathrm{Hei}} = \frac{1}{2}\sum_{\boldsymbol{R},\boldsymbol{R}'}\sum_{\alpha,\beta}\sum_{m,n} J^{mn}_{\alpha\beta}(\boldsymbol{R}'-\boldsymbol{R})\boldsymbol{S}^m_\alpha(\boldsymbol{R})\cdot\boldsymbol{S}^n_\beta(\boldsymbol{R}'), \tag{2}$$

$$\mathcal{H}_{\mathrm{DM}} = \frac{1}{2}\sum_{\boldsymbol{R},\boldsymbol{R}'}\sum_{\alpha}\boldsymbol{D}^{\mathrm{int}}_\alpha(\boldsymbol{R}'-\boldsymbol{R})\cdot\left[\boldsymbol{S}^1_\alpha(\boldsymbol{R})\times\boldsymbol{S}^2_\alpha(\boldsymbol{R}')\right], \tag{3}$$

$$\mathcal{H}_{\mathrm{ext}} = -\sum_{\boldsymbol{R}}\sum_{\alpha=l,r}\left[g\mu_B\boldsymbol{H}\cdot\boldsymbol{S}^m_\alpha(\boldsymbol{R})\right]+\boldsymbol{E}\cdot\boldsymbol{P}^m(\boldsymbol{R}), \tag{4}$$

where the sums in Eqs. (2)–(4) are taken over $\alpha,\beta = l,r$ and the sublattice indices $m,n = 1,2$ ($m\leqslant n$).

In the Hamiltonian $\mathcal{H}_{\mathrm{Hei}}$, $J^{mm}_{lr}(\boldsymbol{0}) = J$ describes the antiferromagnetic intradimer exchange coupling, whereas $J^{mm}_{lr}(\hat{a}) = J_1$ and $J^{mm}_{lr}(2\hat{a}+\hat{c}) = J_2$ are exchange couplings between the spins belonging to the same sublattices [see Fig. 1(a)]. The model also includes Heisenberg interactions between the spins on the different sublattices: $J^{12}_{rr}(\boldsymbol{0}) = J^{12}_{rr}(2\hat{a}+\hat{c}) = J^{12}_{ll}(\hat{b}) = J^{12}_{ll}(2\hat{a}+\hat{b}+\hat{c}) = J_3$ [see Fig. 1(b)]. The Hamiltonian $\mathcal{H}_{\mathrm{Hei}}$ has been studied as a minimal model of $X\mathrm{CuCl_3}$ [3–5]. The Hamiltonian $\mathcal{H}_{\mathrm{DM}}$ in Eq. (3) describes the symmetry-allowed interdimer DM interactions, where $\boldsymbol{D}^{\mathrm{int}}_r(\boldsymbol{0}) = \boldsymbol{D}^{\mathrm{int}}_l(2\hat{a}+\hat{b}+\hat{c}) = D^{\mathrm{int}}\hat{b}$ and $\boldsymbol{D}^{\mathrm{int}}_r(2\hat{a}+\hat{c}) = \boldsymbol{D}^{\mathrm{int}}_l(\hat{b}) = -D^{\mathrm{int}}\hat{b}$ are interdimer DM vectors parallel to the b axis [see Fig. 1(b)] [92]. Here, we do not consider the other components of the interdimer DM vectors allowed by crystal symmetry since their contribution to the thermal Hall effect is negligible. The remaining interactions in Eqs. (2) and (3) are zero. The experimental values of the above mentioned parameters are listed in Table I. Equation (4) describes the Zeeman and polarization terms of $X\mathrm{CuCl_3}$, where $g = 2.06$ for $\boldsymbol{H}\parallel b$ [6], μ_B is the Bohr magneton, and $\boldsymbol{P}^m(\boldsymbol{R})$ is the local polarization on each dimer. To simplify the analysis, we use the coordinate system as $x\parallel\hat{a}+\hat{c}/2$, $y\parallel\hat{a}-\hat{c}/2$, $z\parallel\hat{b}$ where $\hat{a}\perp\hat{b}\perp\hat{c}$, $2a\sim c$, and $2\sqrt{2}a\sim b$ hold approximately for these materials [2] [see Fig. 1(a)].

TABLE I. Experimental values of the interactions (in meV) for $\mathrm{TlCuCl_3}$ [5]. The value of D^{int} remains undetermined [3–5,91].

Parameter	J	J_1	J_2	J_3	D^{int}
Energy	5.5	0.43	3.16	0.91	–

The polarization term in Eq. (4) can be interpreted as the electric field-induced intradimer DM interaction [92]

$$-\boldsymbol{E}\cdot\boldsymbol{P}^m(\boldsymbol{R}) = \boldsymbol{D}^{\mathrm{ext},m}\cdot\left[\boldsymbol{S}^m_l(\boldsymbol{R})\times\boldsymbol{S}^m_r(\boldsymbol{R})\right]. \tag{5}$$

Here the intradimer DM vector $\boldsymbol{D}^{\mathrm{ext},m}$ can be written in terms of the polarization tensor of each sublattice $\tilde{C}^m$ that has nine independent components $C^m_{\mu\nu}$ ($\mu,\nu = x,y,z$) [12–14,93]:

$$D^{\mathrm{ext},m}_\nu = -E_{\mu'}C^m_{\mu'\nu}, \tag{6}$$

where repeated indices are summed over. In the above expression, $D^{\mathrm{ext},m}_\nu$ and E_ν ($\nu = x,y,z$) are the ν component of $\boldsymbol{D}^{\mathrm{ext},m}$ and $\boldsymbol{E}$. The two tensors $C^1_{\mu\nu}$ and $C^2_{\mu\nu}$ are related by [92]

$$C^2_{\mu\nu} = -\gamma_{\mu\mu'}C^1_{\mu'\nu'}\gamma_{\nu\nu'}, \tag{7}$$

where $\gamma = \mathrm{diag}(1,1,-1)$. The experimental values of $C^1_{\mu\nu}$ obtained in the previous studies [14] are listed in Table II. We ignore the z component of the electric field-induced intradimer DM interaction term in the later analysis [94]. In the Supplemental Material [92], we provide a qualitative picture of how the electric field induces the thermal Hall effect in relation to the no-go condition for magnons [28,31,57].

Methods. To study the excitation spectrum of the system, we introduce bond operators $s^{m\dagger}_{\boldsymbol{R}}$ and $t^{m\dagger}_{\boldsymbol{R}\alpha}$ ($\alpha = +,0,-$) that create the singlet state $|s\rangle^m_{\boldsymbol{R}}$ and the three triplet states $|t_\alpha\rangle^m_{\boldsymbol{R}}$ out of the vacuum $|0\rangle^m_{\boldsymbol{R}}$ on each dimer [3–5,96]:

$$\begin{aligned}
|s\rangle^m_{\boldsymbol{R}} &= s^{m\dagger}_{\boldsymbol{R}}|0\rangle^m_{\boldsymbol{R}} = \frac{1}{\sqrt{2}}\left(|\uparrow\downarrow\rangle^m_{\boldsymbol{R}} - |\downarrow\uparrow\rangle^m_{\boldsymbol{R}}\right),\\
|t_+\rangle^m_{\boldsymbol{R}} &= t^{m\dagger}_{\boldsymbol{R}+}|0\rangle^m_{\boldsymbol{R}} = -|\uparrow\uparrow\rangle^m_{\boldsymbol{R}},\\
|t_0\rangle^m_{\boldsymbol{R}} &= t^{m\dagger}_{\boldsymbol{R}0}|0\rangle^m_{\boldsymbol{R}} = \frac{1}{\sqrt{2}}\left(|\uparrow\downarrow\rangle^m_{\boldsymbol{R}} + |\downarrow\uparrow\rangle^m_{\boldsymbol{R}}\right),\\
|t_-\rangle^m_{\boldsymbol{R}} &= t^{m\dagger}_{\boldsymbol{R}-}|0\rangle^m_{\boldsymbol{R}} = |\downarrow\downarrow\rangle^m_{\boldsymbol{R}},
\end{aligned} \tag{8}$$

where $\boldsymbol{R}$ and m denote the position of the unit cell and the sublattice index. These obey Bose statistics and are subject to the constraint $s^{m\dagger}_{\boldsymbol{R}}s^m_{\boldsymbol{R}} + \sum_{\alpha=+,0,-}t^{m\dagger}_{\boldsymbol{R}\alpha}t^m_{\boldsymbol{R}\alpha} = 1$ on each dimer. In the BEC phase, the ground state is well represented by a coherent superposition of the singlet and triplet states on each dimer [5,11]

$$|\mathrm{GS}\rangle^m_{\boldsymbol{R}} = \cos\theta_m|s\rangle^m_{\boldsymbol{R}} + \sin\theta_m\exp(i\phi_m)|t_+\rangle^m_{\boldsymbol{R}}, \tag{9}$$

TABLE II. Experimental values of the polarization tensor $C^1_{\mu\nu}$ (in $\mu\mathrm{C/m^2}$) for $\mathrm{TlCuCl_3}$ [95]. The values of C^1_{zx} and C^1_{zy} are undetermined [11,12,14]. See Supplemental Material for details. The values of C^1_{xz} and C^1_{yz} are not used in our study.

$C^1_{\mu\nu}$	C^1_{xx}	C^1_{xy}	C^1_{yx}	C^1_{yy}	C^1_{zx}	C^1_{zy}	C^1_{zz}
Values	−27.5	−5	−32.5	124.5	–	–	2.5

where θ_m and ϕ_m are variational parameters for each sublattice m. In Eq. (9) and the following analysis, we focus on the high magnetic field regimes $H \geqslant 40\,\mathrm{T}$ for $X = \mathrm{Tl}$ and $H \geqslant 25\,\mathrm{T}$ for $X = \mathrm{K}$ in $X\mathrm{CuCl_3}$, where the contribution of the other two triplet modes to the ground state (9) can be neglected [5].

To analyze the excited states, we perform the following unitary transformation:

$$\begin{aligned} a^{m\dagger}_{\boldsymbol{R}} &= \cos\theta_m s^{m\dagger}_{\boldsymbol{R}} + \sin\theta_m \exp(i\phi_m) t^{m\dagger}_{\boldsymbol{R}+}, \\ b^{m\dagger}_{\boldsymbol{R}+} &= -\sin\theta_m s^{m\dagger}_{\boldsymbol{R}} + \cos\theta_m \exp(i\phi_m) t^{m\dagger}_{\boldsymbol{R}+}, \\ b^{m\dagger}_{\boldsymbol{R}0} &= t^{m\dagger}_{\boldsymbol{R}0}, \\ b^{m\dagger}_{\boldsymbol{R}-} &= t^{m\dagger}_{\boldsymbol{R}-}, \end{aligned} \tag{10}$$

which preserves the particle number constraint, i.e., $a^{m\dagger}_{\boldsymbol{R}} a^{m}_{\boldsymbol{R}} + \sum_{\alpha=+,0,-} b^{m\dagger}_{\boldsymbol{R}\alpha} b^{m}_{\boldsymbol{R}\alpha} = 1$. We follow the standard procedure and replace $a^{m\dagger}_{\boldsymbol{R}} a^{m}_{\boldsymbol{R}}$ with $1 - (1/N)\sum_{\boldsymbol{R},\alpha} b^{m\dagger}_{\boldsymbol{R},\alpha} b^{m}_{\boldsymbol{R},\alpha}$, where N is the number of dimers on the sublattice m. This assumption is justified at low temperatures. By introducing the Fourier transform $b^{m\dagger}_{\boldsymbol{R}\alpha} = 1/N \sum_{\boldsymbol{k}\alpha} b^{m\dagger}_{\boldsymbol{k}\alpha} e^{i\boldsymbol{k}\cdot\boldsymbol{R}^m}$ ($\boldsymbol{R}^1 = \boldsymbol{R}$, and $\boldsymbol{R}^2 = \boldsymbol{R} - (\hat{a} + \hat{b}/2 + \hat{c}/2)$) and retaining only up to quadratic order in $b^{\dagger m}_{\boldsymbol{k}\alpha}$ and $b^{m}_{\boldsymbol{k}\alpha}$, the Hamiltonian (1) takes the form $\mathcal{H} = \mathcal{H}^{(0)} + \mathcal{H}^{(1)} + \mathcal{H}^{(2)}$. Here the constant term $\mathcal{H}^{(0)}$ represents the energy of the variational ground state and $\mathcal{H}^{(1)}$ ($\mathcal{H}^{(2)}$) is the linear (quadratic) term in bosonic operators. The linear term $\mathcal{H}^{(1)}$ vanishes when we choose the parameters θ_m, ϕ_m to minimize $\mathcal{H}^{(0)}$ [92]. The quadratic term $\mathcal{H}^{(2)}$ represents the bosonic Bogoliubov-de Gennes (BdG) Hamiltonian.

Low-energy effective model. Here, we construct the low-energy effective model for ease of analysis. When the magnetic field is strong, the energy of the lowest excitation mode and those of the other two modes are sufficiently separated [92]. For this reason, we consider only the operators $b^{\dagger}_{+}$ and b_{+} to discuss the thermal Hall effect in the high magnetic field and low-temperature regimes. As a result, we obtain the BdG Hamiltonian of the form

$$\mathcal{H}^{(2)} \simeq \frac{1}{2}\sum_{\boldsymbol{k}} \boldsymbol{b}^{\dagger}_{\boldsymbol{k}} H_{\mathrm{BdG}}(\boldsymbol{k}) \boldsymbol{b}_{\boldsymbol{k}}, \tag{11}$$

with a vector $\boldsymbol{b}_{\boldsymbol{k}} = (b^{1}_{\boldsymbol{k}+}, b^{2}_{\boldsymbol{k}+}, b^{1\dagger}_{-\boldsymbol{k}+}, b^{2\dagger}_{-\boldsymbol{k}+})^T$ and the 4×4 matrix

$$H_{\mathrm{BdG}}(\boldsymbol{k}) = \begin{pmatrix} \Xi(\boldsymbol{k}) & \Pi(\boldsymbol{k}) \\ \Pi^*(-\boldsymbol{k}) & \Xi^*(-\boldsymbol{k}) \end{pmatrix}. \tag{12}$$

The explicit expression of the matrix (12) is given in the Supplemental Material [92].

To preserve the bosonic commutation relations, the BdG Hamiltonian (12) has to be diagonalized using a paraunitary matrix $T(\boldsymbol{k})$. The matrix satisfies $T^{\dagger}(\boldsymbol{k})\Sigma_z T(\boldsymbol{k}) = \Sigma_z$, where $\Sigma_z = \mathrm{diag}(1, 1, -1, -1)$. The BdG Hamiltonian is diagonalized as

$$\Sigma_z H_{\mathrm{BdG}}(\boldsymbol{k}) T(\boldsymbol{k}) = T(\boldsymbol{k})\Sigma_z E(\boldsymbol{k}), \tag{13}$$

where the diagonal matrix $E(\boldsymbol{k})$ takes the form $E(\boldsymbol{k}) = \mathrm{diag}(E_1(\boldsymbol{k}), E_2(\boldsymbol{k}), E_1(-\boldsymbol{k}), E_2(-\boldsymbol{k}))$. The positive energies $E_1(\boldsymbol{k})$ and $E_2(\boldsymbol{k})$ correspond to the upper and lower particle bands, respectively. In order to calculate the thermal Hall conductivity, it is sufficient to consider these two bands [32,34].

Thermal Hall effect. We here provide the expression of the three-dimensional thermal Hall conductivity in the z-x plane [34]

$$\kappa_{zx} = -\frac{k_{\mathrm{B}}^2 T}{\hbar}\sum_{n=1}^{2}\int_{\mathrm{BZ}} \frac{d^3k}{(2\pi)^3}\left[c_2(\rho(E_n(\boldsymbol{k}))) - \frac{\pi^2}{3}\right]\Omega^{y}_{n}(\boldsymbol{k}), \tag{14}$$

where $\rho(E_n(\boldsymbol{k})) = 1/(e^{\beta E_n(\boldsymbol{k})} - 1)$ is the Bose distribution function with β being the inverse temperature. The explicit form of $c_2(\rho)$ is given by $c_2(\rho) = (1+\rho)(\log\frac{1+\rho}{\rho})^2 - (\log\rho)^2 - 2\mathrm{Li}_2(-\rho)$, where $\mathrm{Li}_2(x)$ is the dilogarithm function. The Berry curvature of the nth band $\Omega^{y}_{n}(\boldsymbol{k})$ is defined as $\Omega^{y}_{n}(\boldsymbol{k}) = -2\mathrm{Im}[\Sigma_z \frac{\partial T^{\dagger}(\boldsymbol{k})}{\partial k_z}\Sigma_z \frac{\partial T(\boldsymbol{k})}{\partial k_x}]_{nn}$.

Results. Fig. 2 shows the numerical results of κ_{zx} in Eq. (14). In the numerics [97], we set the moderate values of $|\boldsymbol{D}^{\mathrm{int}}|$, C^{1}_{zx}, and C^{1}_{zy} whose values are unknown [see the caption of Fig. 2]

From Fig. 2(a), we find that increasing $|\boldsymbol{E}|$ leads to an enhancement of $|\kappa_{zx}|$. This behavior is consistent with the approximate expression of $|\kappa_{zx}|$, which is discussed in the next section. The obtained values in Fig. 2(a) are comparable to the experimental values of the thermal Hall conductivity of magnons and phonons [29,31,37,51,77] and thus are expected to be experimentally accessible. In addition, the applied electric field whose strength is of the order of $0.1\,\mathrm{MV/cm}$ is realizable in experiments [98].

Figure 2(b) indicates that the sign reversal of E_y results in the sign reversal of κ_{zx}. This result suggests that the direction of the Hall current can be controlled by changing the direction of the electric field in the x-y plane. This can be justified as follows. The sign reversal of E_x and E_y leads to the exchange between $\boldsymbol{D}^{\mathrm{ext},1} \leftrightarrow \boldsymbol{D}^{\mathrm{ext},2}$, and thus the ground-state wave functions of sublattice 1 and 2 [see Eq. (9)] are also swapped. Consequently, when we take complex conjugation of the BdG Hamiltonian (12) with the opposite signs of E_x and E_y and changing the sublattice index as $1 \leftrightarrow 2$, the BdG Hamiltonian almost returns to the original one [99]. This implies that the sign change of E_x and E_y approximately corresponds to the following effective time reversal operation [100]:

$$H_{\mathrm{BdG}}(\boldsymbol{k}) \to P^{\dagger} H^{*}_{\mathrm{BdG}}(-\boldsymbol{k}) P, \quad P = I_{2\times 2} \otimes \sigma_x, \tag{15}$$

which leads to the reversal of the Hall current as shown in Fig. 2(b). The constantlike behavior for $|E_y| \geqslant 0.004\,\mathrm{MV/cm}$ reflects the fact that the ground state (9) does not change much by varying $|E_y|$ due to $|C^{1}_{zy}E_z| \gg |C^{1}_{yy}E_y|$ [101].

We expect qualitatively similar results for $\mathrm{KCuCl_3}$. However, it is more difficult to obtain reliable results in the $\mathrm{KCuCl_3}$ case since there are more undetermined parameters than in the $\mathrm{TlCuCl_3}$ case.

Discussion. Here, we explain how the electric field induces and enhances the thermal Hall effect as in Fig. 2(a). Without an electric field, the difference between the variational parameters $\theta_1 - \theta_2$ and $\phi_1 - \phi_2$ in Eq. (9) are 0 and $\pm\pi$, respectively [3–5]. In this case, the Berry curvature vanishes due to the effective PT symmetry of the BdG Hamiltonian (12). However, the applied electric field gives rise to the difference between θ_1 and θ_2, which breaks the symmetry, resulting in the finite thermal Hall effect [92].

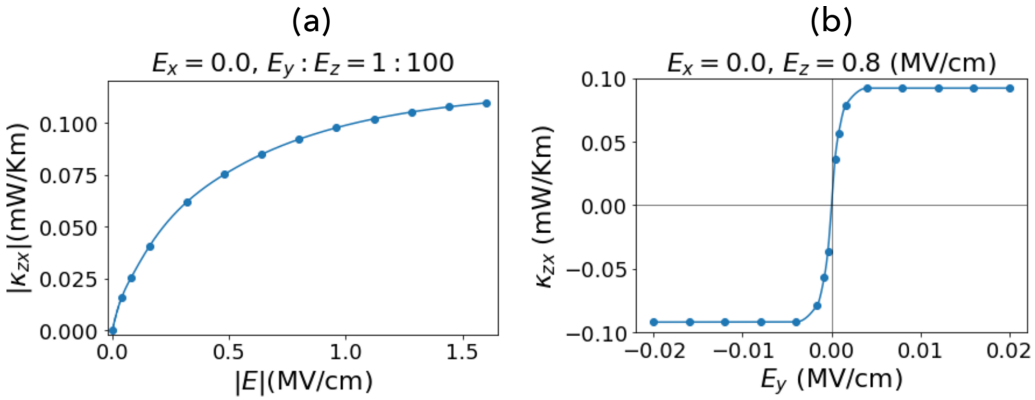

FIG. 2. (a) The absolute value of the thermal Hall conductivity $|\kappa_{zx}|$ as a function of $|\boldsymbol{E}|$ with $E_x = 0.0\,\mathrm{MV/cm}$ and $E_y : E_z = 1 : 100$. (b) κ_{zx} as a function of E_y with $E_x = 0.0\,\mathrm{MV/cm}$ and $E_z = 0.8\,\mathrm{MV/cm}$. The parameters used for (a) and (b) are listed in Tables I and II. We set the moderate values for the undetermined parameters as $D^{\mathrm{int}} = 0.091$ meV, $C^1_{zx} = -16.3\,\mu\mathrm{C/m^2}$, and $C^1_{zy} = 62.3\,\mu\mathrm{C/m^2}$. The magnetic field and temperature are $H = 42\,\mathrm{T}$ and $T = 10\,\mathrm{K}$, respectively.

We now argue that the electric field can open and control the band gap. Before applying the electric field, there are nodal lines $G_{\pm,j}$ in momentum space: $G_{+,j} = (j\pi, k_y, \frac{\pi}{2})$, $G_{-,j} = (\frac{2j-1}{2}\pi, k_y, 0)$ (modulo reciprocal lattice vectors) for $j = 0, 1$, which are protected by the effective PT symmetry [92]. However, the applied electric field breaks the symmetry and opens the band gap at $G_{\pm,j}$ [92], each of which is a source of the Berry curvature as shown in Fig. 3 [102].

For a fixed direction of the electric field, the band gap at $G_{\pm,j}$, which we denote by $E_{\mathrm{gap},\pm,j}(k_y)$, behaves as [92]

$$E_{\mathrm{gap},\pm,j}(k_y) \propto |\boldsymbol{E}|. \tag{16}$$

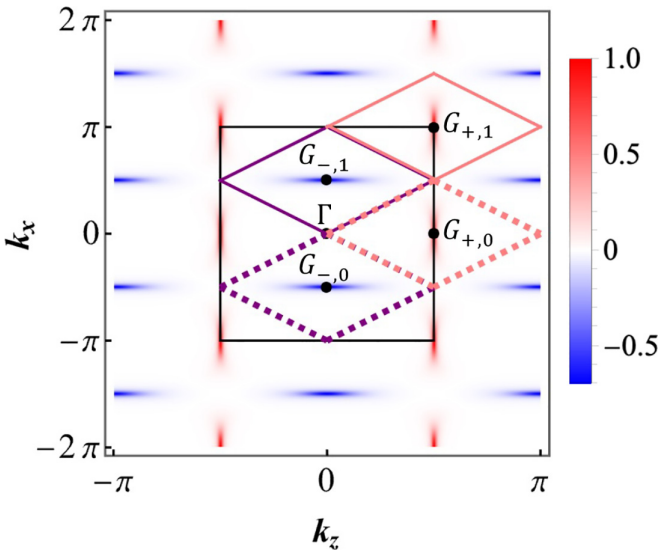

FIG. 3. Distribution of the Berry curvature of the upper band ($n = 1$) in the k_z-k_x plane with $k_y = 0$ under the applied electric field $\boldsymbol{E} = (0.0, 0.016, 1.6)\,\mathrm{MV/cm}$. The area enclosed by the solid black lines denotes the first Brillouin zone (BZ). The areas enclosed by the pink and purple rhombuses indicate the region $S_{+,j}(0)$ and $S_{-,j}(0)$, respectively (the solid ones for $j = 1$ and the dashed ones for $j = 0$).

Let us show that the electric field can increase κ_{zx} by widening the band gap at $G_{\pm,j}$. For a rough estimation, we consider the high-temperature asymptotic form of κ_{zx} in the following. In the temperature region $k_{\mathrm{B}}T \gg E_1(j\pi, k_y, \frac{\pi}{2}), E_1(\frac{2j-1}{2}\pi, k_y, 0)$, we can use the asymptotic form of $c_2(\rho) \sim \frac{\pi^2}{3} - \frac{1}{\rho}$ $(\rho \to \infty)$ [103]. By assuming that the Berry curvature is localized at $G_{\pm,j}$ and using $e^{\beta E_n(\boldsymbol{k})} \simeq 1 + \beta E_n(\boldsymbol{k})$, $\Omega^y_1(\boldsymbol{k}) = -\Omega^y_2(\boldsymbol{k})$, and Eq. (16), we have

$$\begin{aligned}
|\kappa_{zx}| &\simeq \frac{k_{\mathrm{B}}^2 T}{\hbar}\left|\int_{\mathrm{BZ}} \frac{d^3k}{(2\pi)^3}\left[\frac{E_1(\boldsymbol{k}) - E_2(\boldsymbol{k})}{k_{\mathrm{B}}T}\right]\Omega^y_1(\boldsymbol{k})\right| \\
&\simeq \frac{k_{\mathrm{B}}}{8\pi^3\hbar}\left|\sum_{\sigma,j}\int_{k_y} dk_y E_{\mathrm{gap},\sigma,j}(k_y)\int_{S_{\sigma,j}(k_y)} dk_z dk_x \Omega^y_1(\boldsymbol{k})\right| \\
&\simeq \frac{k_{\mathrm{B}}}{8\pi^2\hbar}|E_{\mathrm{gap},+} - E_{\mathrm{gap},-}| \propto |\boldsymbol{E}|,
\end{aligned} \tag{17}$$

where the region $S_{\pm,j}(k_y)$ is the area enclosed by the rhombus around $G_{\pm,j}$ in Fig. 3, and we have defined the average band gaps as $E_{\mathrm{gap},\pm} = \frac{1}{2}\sum_j \int_{k_y} dk_y E_{\mathrm{gap},\pm,j}(k_y)$. In going from the second to the third line, we used $|\int_{S_{\pm,j}(k_y)} dk_z dk_x \Omega^y_1(\boldsymbol{k})| \simeq \frac{\pi}{2}$. Clearly, Eq. (17) shows that $|\kappa_{zx}|$ increases with increasing electric field. Under $H = 42\,\mathrm{T}$ and $\boldsymbol{E} = (0, 0.016, 1.6)\,\mathrm{MV/cm}$, $|\kappa_{zx}|$ in Eq. (17) is estimated as $0.048\,\mathrm{mW/K.m}$, whose order of magnitude is consistent with the numerical result in Fig. 2(a).

Conclusion and outlook. In this Letter, we have proposed the electric field induced thermal Hall effect of triplons in $X\mathrm{CuCl_3}$. We analyzed the isotropic Heisenberg model with symmetry-allowed interdimer and electric field-induced intradimer DM interactions. With this model, we showed that the electric field breaks the effective PT symmetry of the Hamiltonian and thus induces the thermal Hall effect, which can be observed experimentally in realistic electric and magnetic fields. Furthermore, we found that the electric field not only triggers the thermal Hall effect but also opens and enlarges the band gap at nodal lines, which are otherwise protected by the effective PT symmetry without an electric field, thereby enhancing the thermal Hall effect. We also showed

that the sign change of E_x and E_y corresponds to the effective time reversal operation, which reverses the direction of the Hall current.

We anticipate that our proposal stimulates further experimental investigations and offers an approach to manipulating thermal Hall transport. We also expect that our theory should be applicable to a wide class of materials with magnetoelectric coupling. In particular, our approach may prove valuable for lattices whose symmetry properties are heretofore thought to preclude the thermal Hall effect, potentially broadening the research horizon in this field. Finally, if the pressure induces the intradimer DM interaction [104–107], it can play the same role as the electric field.

Acknowledgments. We thank Kosuke Fujiwara, Shojiro Kimura, and Karlo Penc for useful discussions. This work was supported by JSPS KAKENHI Grants No. JP18K03445, No. JP20K14411, No. JP23H01086, No. JP24K00546, MEXT KAKENHI Grant-in-Aid for Scientific Research on Innovative Areas "Quantum Liquid Crystals" (KAK- ENHI Grant No. JP22H04469), and for Transformative Research Areas A "Extreme Universe" (KAKENHI Grant No. JP21H05191). N.E. was supported by Forefront Physics and Mathematics Program to Drive Transformation (FoPM), a World-leading Innovative Graduate Study (WINGS) Program, the University of Tokyo and JSR Fellowship, the University of Tokyo. Y.A. was supported by JST PRESTO Grant No. JPMJPR2251.

[1] T. Nikuni, M. Oshikawa, A. Oosawa, and H. Tanaka, Bose-Einstein condensation of dilute magnons in $TlCuCl_3$, Phys. Rev. Lett. **84**, 5868 (2000).

[2] H. Tanaka, A. Oosawa, T. Kato, H. Uekusa, Y. Ohashi, K. Kakurai, and A. Hoser, Observation of field-induced transverse Néel ordering in the spin gap system $TlCuCl_3$, J. Phys. Soc. Jpn. **70**, 939 (2001).

[3] M. Matsumoto, B. Normand, T. M. Rice, and M. Sigrist, Magnon dispersion in the field-induced magnetically ordered phase of $TlCuCl_3$, Phys. Rev. Lett. **89**, 077203 (2002).

[4] A. Oosawa, T. Takamasu, K. Tatani, H. Abe, N. Tsujii, O. Suzuki, H. Tanaka, G. Kido, and K. Kindo, Field-induced magnetic ordering in the quantum spin system $KCuCl_3$, Phys. Rev. B **66**, 104405 (2002).

[5] M. Matsumoto, B. Normand, T. M. Rice, and M. Sigrist, Field- and pressure-induced magnetic quantum phase transitions in $TlCuCl_3$, Phys. Rev. B **69**, 054423 (2004).

[6] F. Yamada, T. Ono, H. Tanaka, G. Misguich, M. Oshikawa, and T. Sakakibara, Magnetic-field induced Bose–Einstein condensation of magnons and critical behavior in interacting spin dimer system $TlCuCl_3$, J. Phys. Soc. Jpn. **77**, 013701 (2008).

[7] T. Giamarchi, C. Rüegg, and O. Tchernyshyov, Bose-Einstein condensation in magnetic insulators, Nat. Phys. **4**, 198 (2008).

[8] N. Cavadini, G. Heigold, W. Henggeler, A. Furrer, H.-U. Güdel, K. Krämer, and H. Mutka, Magnetic excitations in the quantum spin system $TlCuCl_3$, Phys. Rev. B **63**, 172414 (2001).

[9] N. Cavadini, C. Rüegg, A. Furrer, H.-U. Güdel, K. Krämer, H. Mutka, and P. Vorderwisch, Triplet excitations in low-H_c spin-gap systems $KCuCl_3$ and $TlCuCl_3$: An inelastic neutron scattering study, Phys. Rev. B **65**, 132415 (2002).

[10] C. Rüegg, N. Cavadini, A. Furrer, H. Güdel, K. Krämer, H. Mutka, A. Wildes, K. Habicht, and P. Vorderwisch, Bose–Einstein condensation of the triplet states in the magnetic insulator $TlCuCl_3$, Nature (London) **423**, 62 (2003).

[11] S. Kimura, K. Kakihata, Y. Sawada, K. Watanabe, M. Matsumoto, M. Hagiwara, and H. Tanaka, Ferroelectricity by Bose-Einstein condensation in a quantum magnet, Nat. Commun. **7**, 12822 (2016).

[12] S. Kimura, K. Kakihata, Y. Sawada, K. Watanabe, M. Matsumoto, M. Hagiwara, and H. Tanaka, Magnetoelectric effect in the quantum spin gap system $TlCuCl_3$, Phys. Rev. B **95**, 184420 (2017).

[13] S. Kimura, M. Matsumoto, M. Akaki, M. Hagiwara, K. Kindo, and H. Tanaka, Electric dipole spin resonance in a quantum spin dimer system driven by magnetoelectric coupling, Phys. Rev. B **97**, 140406(R) (2018).

[14] S. Kimura, M. Matsumoto, and H. Tanaka, Electrical switching of the nonreciprocal directional microwave response in a triplon Bose-Einstein condensate, Phys. Rev. Lett. **124**, 217401 (2020).

[15] R. Ramesh and N. A. Spaldin, Multiferroics: progress and prospects in thin films, Nat. Mater. **6**, 21 (2007).

[16] S.-W. Cheong and M. Mostovoy, Multiferroics: a magnetic twist for ferroelectricity, Nat. Mater. **6**, 13 (2007).

[17] M. Bibes and A. Barthélémy, Towards a magnetoelectric memory, Nat. Mater. **7**, 425 (2008).

[18] T. Liu and G. Vignale, Electric control of spin currents and spin-wave logic, Phys. Rev. Lett. **106**, 247203 (2011).

[19] Y. Tokura, S. Seki, and N. Nagaosa, Multiferroics of spin origin, Rep. Prog. Phys. **77**, 076501 (2014).

[20] H. Yang, O. Boulle, V. Cros, A. Fert, and M. Chshiev, Controlling Dzyaloshinskii-Moriya interaction via chirality dependent atomic-layer stacking, insulator capping and electric field, Sci. Rep. **8**, 12356 (2018).

[21] W. Zhang, H. Zhong, R. Zang, Y. Zhang, S. Yu, G. Han, G. L. Liu, S. S. Yan, S. Kang, and L. M. Mei, Electrical field enhanced interfacial Dzyaloshinskii-Moriya interaction in MgO/Fe/Pt system, Appl. Phys. Lett. **113**, 122406 (2018).

[22] T. Srivastava, M. Schott, R. Juge, V. Krizakova, M. Belmeguenai, Y. Roussigné, A. Bernand-Mantel, L. Ranno, S. Pizzini, S.-M. Chérif *et al.*, Large-voltage tuning of Dzyaloshinskii–Moriya interactions: A route toward dynamic control of skyrmion chirality, Nano Lett. **18**, 4871 (2018).

[23] B. Rana and Y. Otani, Towards magnonic devices based on voltage-controlled magnetic anisotropy, Commun. Phys. **2**, 90 (2019).

[24] C.-K. Li, X.-P. Yao, and G. Chen, Writing and deleting skyrmions with electric fields in a multiferroic heterostructure, Phys. Rev. Res. **3**, L012026 (2021).

[25] S. Mankovsky, E. Simon, S. Polesya, A. Marmodoro, and H. Ebert, Electric-field control of exchange interactions, Phys. Rev. B **104**, 174443 (2021).

[26] C. Huang, L. Z. Jiang, Y. Zhu, Y. F. Pan, J. Y. Fan, C. L. Ma, J. Hu, and D. N. Shi, Tuning Dzyaloshinskii–Moriya interaction via an electric field at the Co/h-BN interface, Phys. Chem. Chem. Phys. **23**, 22246 (2021).

[27] J. Richter, V. Ohanyan, J. Schulenburg, and J. Schnack, Electric field driven flat bands: Enhanced magnetoelectric and electrocaloric effects in frustrated quantum magnets, Phys. Rev. B **105**, 054420 (2022).

[28] H. Katsura, N. Nagaosa, and P. A. Lee, Theory of the thermal Hall effect in quantum magnets, Phys. Rev. Lett. **104**, 066403 (2010).

[29] Y. Onose, T. Ideue, H. Katsura, Y. Shiomi, N. Nagaosa, and Y. Tokura, Observation of the magnon Hall effect, Science **329**, 297 (2010).

[30] R. Matsumoto and S. Murakami, Theoretical prediction of a rotating magnon wave packet in ferromagnets, Phys. Rev. Lett. **106**, 197202 (2011).

[31] T. Ideue, Y. Onose, H. Katsura, Y. Shiomi, S. Ishiwata, N. Nagaosa, and Y. Tokura, Effect of lattice geometry on magnon Hall effect in ferromagnetic insulators, Phys. Rev. B **85**, 134411 (2012).

[32] R. Shindou, R. Matsumoto, S. Murakami, and J. I. Ohe, Topological chiral magnonic edge mode in a magnonic crystal, Phys. Rev. B **87**, 174427 (2013).

[33] L. Zhang, J. Ren, J.-S. Wang, and B. Li, Topological magnon insulator in insulating ferromagnet, Phys. Rev. B **87**, 144101 (2013).

[34] R. Matsumoto, R. Shindou, and S. Murakami, Thermal hall effect of magnons in magnets with dipolar interaction, Phys. Rev. B **89**, 054420 (2014).

[35] A. Mook, J. Henk, and I. Mertig, Edge states in topological magnon insulators, Phys. Rev. B **90**, 024412 (2014).

[36] A. Mook, J. Henk, and I. Mertig, Magnon Hall effect and topology in kagome lattices: A theoretical investigation, Phys. Rev. B **89**, 134409 (2014).

[37] M. Hirschberger, R. Chisnell, Y. S. Lee, and N. P. Ong, Thermal Hall effect of spin excitations in a kagome magnet, Phys. Rev. Lett. **115**, 106603 (2015).

[38] R. Chisnell, J. S. Helton, D. E. Freedman, D. K. Singh, R. I. Bewley, D. G. Nocera, and Y. S. Lee, Topological magnon bands in a kagome lattice ferromagnet, Phys. Rev. Lett. **115**, 147201 (2015).

[39] B. Xu, T. Ohtsuki, and R. Shindou, Integer quantum magnon Hall plateau-plateau transition in a spin-ice model, Phys. Rev. B **94**, 220403(R) (2016).

[40] R. Cheng, S. Okamoto, and D. Xiao, Spin Nernst effect of magnons in collinear antiferromagnets, Phys. Rev. Lett. **117**, 217202 (2016).

[41] V. A. Zyuzin and A. A. Kovalev, Magnon spin Nernst effect in antiferromagnets, Phys. Rev. Lett. **117**, 217203 (2016).

[42] S. K. Kim, H. Ochoa, R. Zarzuela, and Y. Tserkovnyak, Realization of the Haldane-Kane-Mele model in a system of localized spins, Phys. Rev. Lett. **117**, 227201 (2016).

[43] Y. Shiomi, R. Takashima, and E. Saitoh, Experimental evidence consistent with a magnon Nernst effect in the antiferromagnetic insulator $MnPS_3$, Phys. Rev. B **96**, 134425 (2017).

[44] P. Laurell and G. A. Fiete, Topological magnon bands and unconventional superconductivity in pyrochlore iridate thin films, Phys. Rev. Lett. **118**, 177201 (2017).

[45] K. Nakata, J. Klinovaja, and D. Loss, Magnonic quantum Hall effect and Wiedemann-Franz law, Phys. Rev. B **95**, 125429 (2017).

[46] K. Nakata, S. K. Kim, J. Klinovaja, and D. Loss, Magnonic topological insulators in antiferromagnets, Phys. Rev. B **96**, 224414 (2017).

[47] S. A. Owerre, Topological thermal Hall effect in frustrated kagome antiferromagnets, Phys. Rev. B **95**, 014422 (2017).

[48] S. Murakami and A. Okamoto, Thermal Hall effect of magnons, J. Phys. Soc. Jpn. **86**, 011010 (2017).

[49] P. Laurell and G. A. Fiete, Magnon thermal Hall effect in kagome antiferromagnets with Dzyaloshinskii-Moriya interactions, Phys. Rev. B **98**, 094419 (2018).

[50] T. Cookmeyer and J. E. Moore, Spin-wave analysis of the low-temperature thermal Hall effect in the candidate Kitaev spin liquid α-$RuCl_3$, Phys. Rev. B **98**, 060412(R) (2018).

[51] H. Doki, M. Akazawa, H.-Y. Lee, J. H. Han, K. Sugii, M. Shimozawa, N. Kawashima, M. Oda, H. Yoshida, and M. Yamashita, Spin thermal Hall conductivity of a kagome antiferromagnet, Phys. Rev. Lett. **121**, 097203 (2018).

[52] P. A. McClarty, X.-Y. Dong, M. Gohlke, J. G. Rau, F. Pollmann, R. Moessner, and K. Penc, Topological magnons in Kitaev magnets at high fields, Phys. Rev. B **98**, 060404(R) (2018).

[53] D. G. Joshi, Topological excitations in the ferromagnetic Kitaev-Heisenberg model, Phys. Rev. B **98**, 060405(R) (2018).

[54] V. A. Zyuzin and A. A. Kovalev, Spin Hall and Nernst effects of Weyl magnons, Phys. Rev. B **97**, 174407 (2018).

[55] A. Mook, J. Henk, and I. Mertig, Thermal Hall effect in noncollinear coplanar insulating antiferromagnets, Phys. Rev. B **99**, 014427 (2019).

[56] H. Kondo, Y. Akagi, and H. Katsura, $\mathbb{Z}_2$ topological invariant for magnon spin Hall systems, Phys. Rev. B **99**, 041110(R) (2019).

[57] M. Kawano and C. Hotta, Thermal Hall effect and topological edge states in a square-lattice antiferromagnet, Phys. Rev. B **99**, 054422 (2019).

[58] H. Kondo, Y. Akagi, and H. Katsura, Three-dimensional topological magnon systems, Phys. Rev. B **100**, 144401 (2019).

[59] S. K. Kim, K. Nakata, D. Loss, and Y. Tserkovnyak, Tunable magnonic thermal Hall effect in skyrmion crystal phases of ferrimagnets, Phys. Rev. Lett. **122**, 057204 (2019).

[60] K. Hwang, N. Trivedi, and M. Randeria, Topological magnons with nodal-line and triple-point degeneracies: Implications for thermal Hall effect in pyrochlore iridates, Phys. Rev. Lett. **125**, 047203 (2020).

[61] Y. Akagi, Topological invariant for bosonic Bogoliubov–de Gennes systems with disorder, J. Phys. Soc. Jpn. **89**, 123601 (2020).

[62] H. Kondo, Y. Akagi, and H. Katsura, Non-Hermiticity and topological invariants of magnon Bogoliubov–de Gennes systems, Prog. Theor. Exp. Phys. **2020**, 12A104 (2020).

[63] K. Nakata and S. K. Kim, Topological Hall effects of magnons in ferrimagnets, J. Phys. Soc. Jpn. **90**, 081004 (2021).

[64] H. Kondo and Y. Akagi, Dirac surface states in magnonic analogs of topological crystalline insulators, Phys. Rev. Lett. **127**, 177201 (2021).

[65] K. Fujiwara, S. Kitamura, and T. Morimoto, Thermal Hall responses in frustrated honeycomb spin systems, Phys. Rev. B **106**, 035113 (2022).

[66] H. Kim and S. K. Kim, Topological phase transition in magnon bands in a honeycomb ferromagnet driven by sublattice symmetry breaking, Phys. Rev. B **106**, 104430 (2022).

[67] P. A. McClarty, Topological magnons: A review, Annu. Rev. Condens. Matter Phys. **13**, 171 (2022).

[68] R. R. Neumann, A. Mook, J. Henk, and I. Mertig, Thermal Hall effect of magnons in collinear antiferromagnetic insulators: Signatures of magnetic and topological phase transitions, Phys. Rev. Lett. **128**, 117201 (2022).

[69] G. Go, D. An, H.-W. Lee, and S. K. Kim, Magnon orbital Nernst effect in honeycomb antiferromagnets without spin–orbit coupling, Nano Lett. **24**, 5968 (2024).

[70] F. Zhuo, J. Kang, A. Manchon, and Z. Cheng, Topological phases in magnonics, Adv. Phys. Res., 2300054 (2023).

[71] X.-T. Zhang, Y. H. Gao, and G. Chen, Thermal Hall effects in quantum magnets, Phys. Rep. **1070**, 1 (2024).

[72] S. Raghu and F. D. M. Haldane, Analogs of quantum-Hall-effect edge states in photonic crystals, Phys. Rev. A **78**, 033834 (2008).

[73] A. Petrescu, A. A. Houck, and K. Le Hur, Anomalous Hall effects of light and chiral edge modes on the Kagomé lattice, Phys. Rev. A **86**, 053804 (2012).

[74] M. C. Rechtsman, J. M. Zeuner, Y. Plotnik, Y. Lumer, D. Podolsky, F. Dreisow, S. Nolte, M. Segev, and A. Szameit, Photonic Floquet topological insulators, Nature (London) **496**, 196 (2013).

[75] M. Hafezi, S. Mittal, J. Fan, A. Migdall, and J. M. Taylor, Imaging topological edge states in silicon photonics, Nat. Photon. **7**, 1001 (2013).

[76] P. Ben-Abdallah, Photon thermal Hall effect, Phys. Rev. Lett. **116**, 084301 (2016).

[77] C. Strohm, G. L. J. A. Rikken, and P. Wyder, Phenomenological evidence for the phonon Hall effect, Phys. Rev. Lett. **95**, 155901 (2005).

[78] L. Sheng, D. N. Sheng, and C. S. Ting, Theory of the phonon Hall effect in paramagnetic dielectrics, Phys. Rev. Lett. **96**, 155901 (2006).

[79] Y. Kagan and L. A. Maksimov, Anomalous Hall effect for the phonon heat conductivity in paramagnetic dielectrics, Phys. Rev. Lett. **100**, 145902 (2008).

[80] L. Zhang, J. Ren, J.-S. Wang, and Baowen Li, Topological nature of the phonon Hall effect, Phys. Rev. Lett. **105**, 225901 (2010).

[81] L. Zhang, J. Ren, J.-S. Wang, and B. Li, The phonon Hall effect: theory and application, J. Phys.: Condens. Matter **23**, 305402 (2011).

[82] T. Qin, J. Zhou, and J. Shi, Berry curvature and the phonon Hall effect, Phys. Rev. B **86**, 104305 (2012).

[83] J. Romhányi, K. Penc, and R. Ganesh, Hall effect of triplons in a dimerized quantum magnet, Nat. Commun. **6**, 6805 (2015).

[84] M. Malki and K. P. Schmidt, Magnetic Chern bands and triplon Hall effect in an extended Shastry-Sutherland model, Phys. Rev. B **95**, 195137 (2017).

[85] P. A. McClarty, F. Krüger, T. Guidi, S. F. Parker, K. Refson, A. W. Parker, D. Prabhakaran, and R. Coldea, Topological triplon modes and bound states in a Shastry–Sutherland magnet, Nat. Phys. **13**, 736. (2017).

[86] D. G. Joshi and A. P. Schnyder, $\mathbb{Z}_2$ topological quantum paramagnet on a honeycomb bilayer, Phys. Rev. B **100**, 020407(R) (2019).

[87] H. Sun, P. Sengupta, D. Nam, and B. Yang, Negative thermal Hall conductance in a two-dimer Shastry-Sutherland model with a π-flux Dirac triplon, Phys. Rev. B **103**, L140404 (2021).

[88] D. Bhowmick and P. Sengupta, Weyl triplons in $SrCu_2(BO_3)_2$, Phys. Rev. B **104**, 085121 (2021).

[89] S. Suetsugu, T. Yokoi, K. Totsuka, T. Ono, I. Tanaka, S. Kasahara, Y. Kasahara, Z. Chengchao, H. Kageyama, and Y. Matsuda, Intrinsic suppression of the topological thermal Hall effect in an exactly solvable quantum magnet, Phys. Rev. B **105**, 024415 (2022).

[90] A. Thomasen, K. Penc, N. Shannon, and J. Romhányi, Fragility of $\mathbb{Z}_2$ topological invariant characterizing triplet excitations in a bilayer kagome magnet, Phys. Rev. B **104**, 104412 (2021).

[91] T. Saha-Dasgupta and R. Valenti, Comparative study between two quantum spin systems $KCuCl_3$ and $TlCuCl_3$, Europhys. Lett. **60**, 309 (2002).

[92] See Supplemental Material at http://link.aps.org/supplemental/10.1103/PhysRevResearch.6.L032050 for details.

[93] T. A. Kaplan and S. D. Mahanti, Canted-spin-caused electric dipoles: A local symmetry theory, Phys. Rev. B **83**, 174432 (2011).

[94] In the later analysis, we only focus on the lowest triplon mode. Since the z component of the electric field-induced intradimer DM interaction term barely affects the lowest mode, we can ignore the z component in the present analysis.

[95] The values in Table II are taken from [14]. Although the values in Table II look different from the values in [14], they are consistent if we use the same coordinate system as in [14].

[96] S. Sachdev and R. N. Bhatt, Bond-operator representation of quantum spins: Mean-field theory of frustrated quantum heisenberg antiferromagnets, Phys. Rev. B **41**, 9323 (1990).

[97] We used the method of Ref. [108].

[98] T. Lottermoser, T. Lonkai, U. Amann, D. Hohlwein, J. Ihringer, and M. Fiebig, Magnetic phase control by an electric field, Nature (London) **430**, 541 (2004).

[99] The BdG Hamiltonian does not exactly return to the original one if $\phi_2 - \phi_1 \neq \pm\pi$. However, the difference from $\pm\pi$ is usually small enough to be neglected.

[100] The qualitative explanation is as follows. The swapping between the ground state of sublattice 1 and 2 effectively corresponds to the sign change of the symmetry-allowed interdimer DM interaction due to its antisymmetry. This leads to the reversal of fictitious fluxes induced by the interdimer DM interaction (see also the Supplemental Material for the explanation of fictitious fluxes), resulting in the time reversal operation.

[101] The ground state (9) drastically changes around $|E_y| = 0$, where κ_{zx} shows a sharp change.

[102] As expected from Fig. 3, the Chern numbers for these two bands are zero. Nonetheless, the thermal Hall effect can manifest owing to the bosonic nature, i.e., thermally excited triplons contribute to the thermal Hall conductivity through the Bose distribution function $\rho(E_n(\boldsymbol{k})) = 1/(e^{\beta E_n(\boldsymbol{k})} - 1)$ as seen in Eq. (14).

[103] R. Samajdar, S. Chatterjee, S. Sachdev, and M. S. Scheurer, Thermal Hall effect in square-lattice spin liquids: A Schwinger boson mean-field study, Phys. Rev. B **99**, 165126 (2019).

[104] O. M. Volkov, D. D. Sheka, Y. Gaididei, V. P. Kravchuk, U. K. Rößler, J. Fassbender, and D. Makarov, Mesoscale Dzyaloshinskii-Moriya interaction: geometrical tailoring of the magnetochirality, Sci. Rep. **8**, 866 (2018).

[105] S. Qi, J. Jiang, and W. Mi, Tunable valley polarization, magnetic anisotropy and Dzyaloshinskii–Moriya interaction in two-dimensional intrinsic ferromagnetic Janus 2H-VSeX (X = S, Te) monolayers, Phys. Chem. Chem. Phys. **22**, 23597 (2020).

[106] C. Xu, Q.-J. Wang, B. Xu, and J. Hu, Effect of biaxial strain and hydrostatic pressure on the magnetic properties of bilayer CrI_3, Front. Phys. **16**, 53502 (2021).

[107] Y. Xing, H. Chen, N. Xu, X. Li, and L. Zhang, Valley modulation and single-edge transport of magnons in breathing kagome ferromagnets, Phys. Rev. B **105**, 104409 (2022).

[108] T. Fukui, Y. Hatsugai, and H. Suzuki, Chern numbers in discretized Brillouin zone: Efficient method of computing (spin) Hall conductances, J. Phys. Soc. Jpn. **74**, 1674 (2005).